STRUCTURAL CONTROL AND HEALTH MONITORING
Struct. Control Health Monit. (2016)
Published online in Wiley Online Library (wileyonlinelibrary.com). DOI: 10.1002/stc.1872

Distributed sensing of a masonry vault during nearby piling

Sinan Acikgoz[1,*,†], Loizos Pelecanos[1], Giorgia Giardina[2], James Aitken[3] and Kenichi Soga[1]

[1]*Cambridge Centre for Smart Infrastructure and Construction, University of Cambridge, Cambridge, UK*
[2]*Department of Engineering, University of Cambridge, Cambridge, UK*
[3]*London Bridge Station Redevelopment Project, London, UK*

SUMMARY

Piles were constructed inside historic brick barrel vaults during the London Bridge Station Redevelopment. In order to ensure safe operation of the tracks above, movements of the vaults were monitored regularly by total stations. Concurrently, two distributed sensing technologies, fibre optic cables and laser scanners, were used to investigate the vault response to settlements. This paper discusses the monitoring data retrieved from these 'point' and 'distributed' sensing technologies and evaluates their use in structural assessment. The total station data are examined first. It is characterized by high precision and limited spatial coverage due to the use of optical targets. As a result, the total station data are useful for threshold detection but do not provide a detailed understanding of structural response or damage. In contrast, by utilizing distributed fibre optic sensors based on Brillouin optical domain reflectometry, the strain development in the structure during piling is quantified. The location and width of resulting crack openings are also determined, providing useful indicators for damage evaluation. The comparison of point clouds from laser scanners obtained at different stages of pile construction further expands the spatial coverage by detecting global movement of the structure on all visible surfaces. Using these data, the two hinge-response mechanism of the vault is revealed. The rich distributed data enable the calibration of the 2D mechanism and the finite element models, elucidating the contribution of arch stiffness, arch and backfill interaction, potential lateral movements and inter-ring sliding to the response. © 2016 The Authors. Structural Control and Health Monitoring published by John Wiley & Sons, Ltd.

Received 8 January 2016; Revised 22 March 2016; Accepted 29 March 2016

KEY WORDS: distributed sensing; fibre optics; laser scanning; cloud comparison; masonry arch bridge; settlement

1. INTRODUCTION

Engineers were faced with the task of predicting the response of historic brick vaults to piling-induced settlements during the London Bridge Station Redevelopment (LBSR) project. Piling works were carried out inside vaults under the operational platforms and tracks. In earlier phases of the project, the disturbance of the ground and changes in the subsurface hydraulic conditions during piling caused appreciable ground settlements. However, local ground conditions and different piling methods led to a large variability in observed settlements [1]. The engineers' task was made more difficult by the challenges in modelling of arches. Typically, the arches respond to foundation settlements by forming hinges and sliding interfaces between bricks. Modelling these phenomena accurately requires detailed information on the interaction of brick and mortar assemblies [2]. Despite extensive *in situ* investigations, uncertainties existed regarding geometry, materials and the existing defects in the arches as well as the magnitude of expected ground movements [3]. These aspects made a reliable prediction of the settlement response of vaults difficult.

*Correspondence to: Sinan Acikgoz, Department of Engineering, University of Cambridge, Trumpington Street, Cambridge, CB2 1PZ, UK.
†E-mail: msa44@cam.ac.uk

To reduce the risk due to uncertainties, monitoring of settlements and arch response was necessary. This was achieved using total stations, which tracked the position of an array of optical targets attached at selected locations of the arch. To provide further information, two other systems were trialled. The distributed fibre optic sensor system, which utilizes the technique of Brillouin optical time domain reflectometry (BOTDR), was used to investigate the strain development at several sections along the arch. The laser scanning system was used to generate georeferenced 3D point clouds before and after piling, which were compared with provide global deformation estimations for all visible surfaces.

This paper discusses the data gathered from these 'point' and 'distributed' sensors for a particular vault in the London Bridge station. The main objectives of this paper are to evaluate the distributed monitoring data and explore its use in understanding the structural response better. First, the monitored vault and the associated construction works are described in Section 2. Then in Sections 3, 4 and 5, the aforementioned three sensing technologies and data analysis techniques are discussed. For each sensing technology, a brief overview of each technology is followed by a detailed examination of the gathered data. In these sections, by comparing data from different sources, the validation of sensors and data analysis techniques is achieved. Then, in Section 6, the settlement responses simulated by a 2D mechanism and a finite element model are examined. By comparing the simulation and monitoring results, the contribution of various structural characteristics to the response is investigated. Finally, Section 7 summarizes the conclusions obtained in this study.

2. THE MONITORED STRUCTURE

The London Bridge station is one of the oldest stations in London. The first masonry viaducts carrying the tracks were constructed as early as 1836. Later, the station expanded in multiple phases of development in the 19th century and reached its current borders by 1893 [4]. The changes in building materials and vaulting techniques over the 19th century resulted in constructions of different structural characteristics.

The vault that is examined in this paper lies at the northern edge of the site (plan view in Figure 1, left). In plan, it is approximately 12.5 m wide and 17.5 m long and exhibits a slight skew of 1.5°. This barrel vault, which will be referred to as E951N, was constructed in the final phase of expansion of the station in 1893 alongside bordering vaults E950 and E952, to carry two additional tracks (tracks 1 and 2 in Figure 1, left). The southern section of E951, which will be referred to as E951S, was constructed in 1867. Finally, to the north of E951N lie the historic offices of the South Eastern Railway Company.

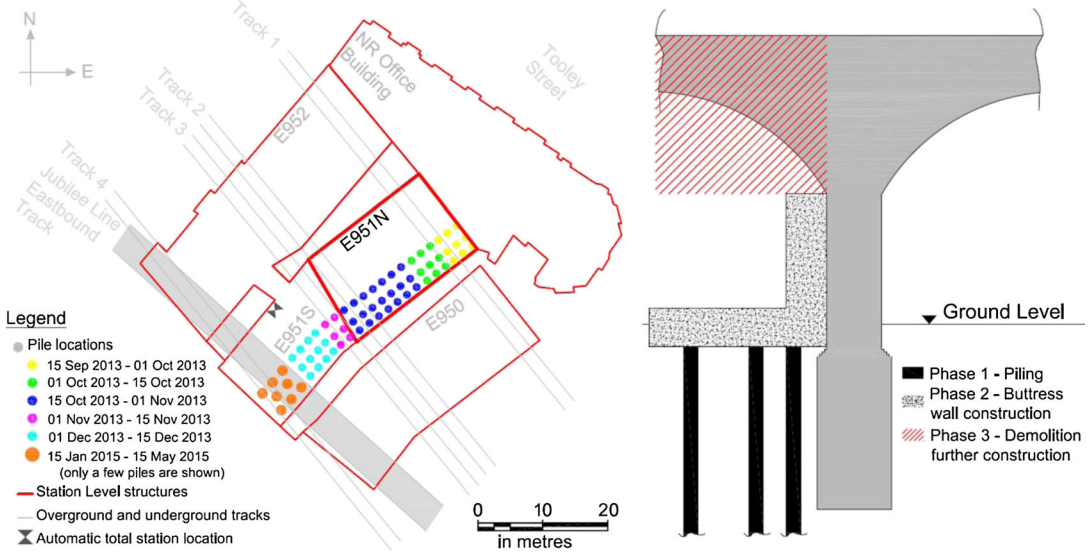

Figure 1. Plan view (left) and cross-sectional view (right) of the monitored arch E951N illustrating the associated construction works.

DOI: 10.1002/stc

The LBSR project is a part of the Thameslink upgrade, which will increase the capacity of the north–south London routes. Within this framework, the main objective of the LBSR project is to increase the number of through tracks and extend the capacity of the platforms. This required demolition of several historic vault structures, and the construction of new viaducts and a new concourse was planned. However, in order to keep part of the station operational during the works, a strict sequence of works had to be followed.

Figure 1 (right) illustrates the sequence of the construction works that was designed for arch E951N. In the first phase, piles were constructed in the arch, which ran parallel to the existing masonry piers. The piles were constructed sequentially in the period September to November 2013 (Figure 1, left, and Figure 2, top right). Then, a buttress wall was constructed by casting the pile caps and a wall that is flush to the existing masonry pier (Figure 2, bottom right). At the time of writing this paper, this is the current stage of the construction and the buttress walls are yet to be cast. The demolition of the masonry piers to the west will follow in the next stage. Then, the lateral thrust forces from Arch E950 will be transmitted to the buttress wall and the piled foundations, ensuring the stability of the remaining brick viaducts and allowing further construction.

Figure 2 provides a longitudinal section cut through vault E951N. The arches were constructed on shallow lime concrete footings, which penetrate layers of made ground and soft alluvium. The alluvium bears onto a 7-m-thick layer of River Terrace Gravels. The 1.7-m-wide piers were constructed on the footings and were made wholly of bricks. The segmental arch constructed on top of the piers had an angle of embrace of 120°, a span of 10.9 m, a span/depth ratio of 2.8 and a thickness to depth ratio of 0.2. It was constructed from six rings of half bricks arranged in stretchers. Semi-hydraulic lime mortar was utilized to bond the bricks in and between the rings. The arch was supported by a 2.4-m-deep backing. A layer of lime concrete fill covered the space between the top of the backing and crown extrados. There was significant uncertainty regarding the material characteristics of this fill. Above the lime concrete, a metre of compacted earth and ballasted tracks is found. Visual assessments were carried out before piling in E951N. No notable crack formations were observed.

In the period from September to December 2013, 57 piles were constructed in arch E951. Thirty-nine of these piles were constructed in E951N, and on average, a single pile was constructed per day. All of these piles are end-bearing 450-mm-diameter piles that terminate in London Clay. All piles were constructed using the Segmental Flight Auger piling technique using low-headroom piling rigs.

Piles were constructed successfully and on schedule. Visual assessments were carried out during and after the piling work in E951N. No significant cracks formed, and the piling operation did not affect the track operation. As will be discussed in Section 3, the total station monitoring system reported centimetre-order movements in E951N. In comparison, the movements that were observed

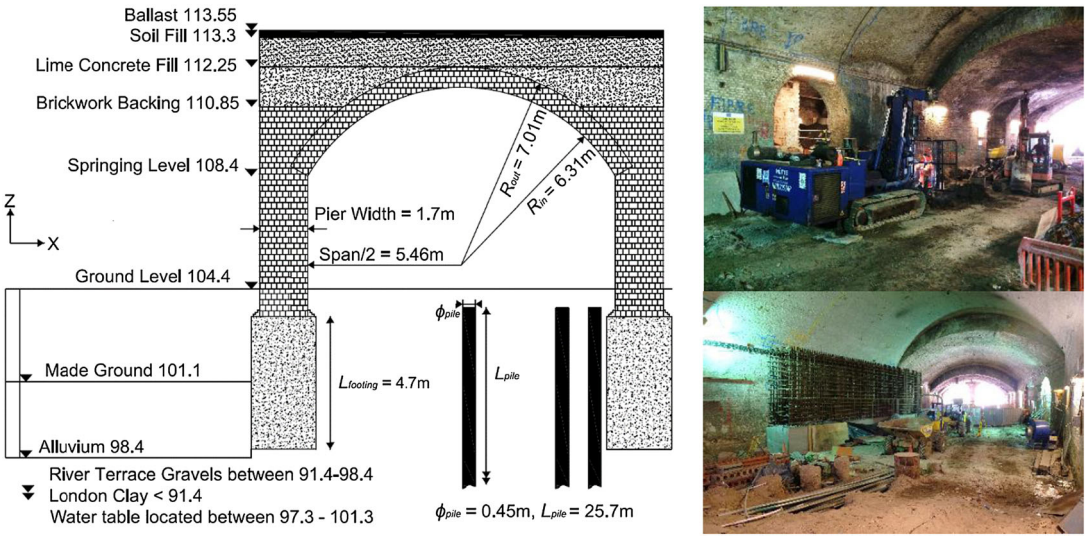

Figure 2. Scaled drawing of a longitudinal cross-section of arch E951N with important dimensions and London grid levels (left) and photos showing the arch and the piling works (right).

DOI: 10.1002/stc

later during the casting of the pile cap (March–April 2014) and piling in E951S (January–May 2015) were negligible. Therefore, while the next sections examine the data gathered between August 2013 and June 2015, the focus remains on the structural response to piling-induced settlements.

3. POINT MONITORING USING TOTAL STATIONS

Total stations are precision measurement devices equipped with a laser beam and a precise servomotor. They emit a modulated wave, which is reflected from optical targets. From the characteristics of the reflection and total station orientation, the device determines the centre of the optical target and its relative location [5]. In the LBSR project, these distances are georeferenced (i.e. converted into global coordinates), by initially determining the position of the device with respect to control points, which have known global coordinates [6].

In the LBSR project, the monitoring activity was concentrated on two levels and carried out by the contractor (Figure 3). Measurements were taken on the track level, to monitor changes in track cant, gauge and twist during piling works. These measurements are outside the scope of this study and will not be discussed. Further monitoring was carried out at the station level vault structures. Two optical targets were placed at the springing points along the arch longitudinal axis, to monitor the settlement of the pier walls. Another optical target was placed at the crown of the arch to monitor the arch distortion due to settlements [6–8]. In arch E951N, these were deployed for three longitudinal sections (Figure 3, middle). Three control targets were located northeast from E951N, and other control targets were placed towards the south and southeast (not shown). During the project, relative movements were detected in several of these control points (e.g. control points at the southern end of E951S), resulting in their elimination from the calculations.

Both manual and automatic (robotic) total stations were used to monitor the movement of the optical targets. During the piling work in E951N, the arch was surveyed using Leica TS15 daily or weekly. According to the manufacturer, the device is accurate to 1 mm in distance measurement and 1 arc sec in angle measurement (accuracy is defined as one standard deviation [9]). Later, in February 2014, a Leica TS50 robotic total station was deployed in the northwest corner of arch E951S (shown in Figure 1, left) to allow hourly automatic monitoring of optical targets. This device is accurate to 0.6 mm in distance measurement and 0.5 arc sec in angle measurement (accuracy defined as above in [10]). Figure 3 (right row) shows the device and the round optical prism targets in the background.

Figure 4 shows an example of processed movement data from a set of targets lying on the north eastern corner of arch E951N (see the highlighted optical prism targets specified in Figure 3). The processed movement data are calculated from changes in global coordinates. In addition, offsets are applied on the data to remove external disturbances to the targets such as accidental knocking of prisms during construction works. Although surveyors make a significant effort to remove external disturbances to capture the true movement of the structure, it is possible to spot displacement spikes in Figure 4 owing to external disturbances. It is also noticed that in the manual monitoring system, daily fluctuations of 3 mm could be observed. After the switch to the automatic system, the typical daily fluctuations reduce to around 0.5 mm.

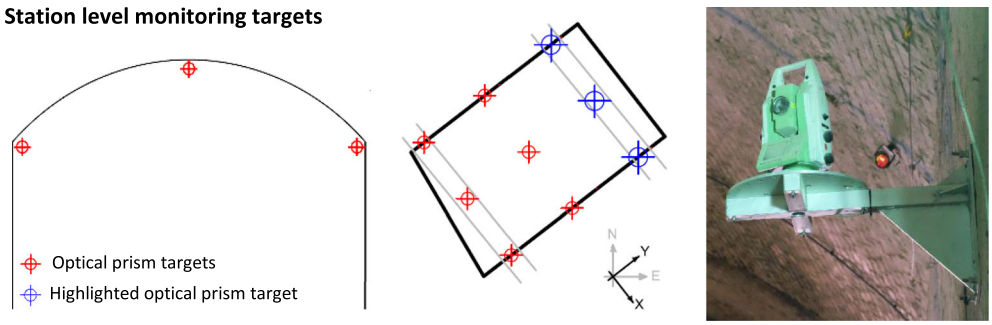

Figure 3. Schematic of the monitoring targets in arch E951N in section view (left) and in plan view (middle). In the right, the photo shows the automatic total station and an optical prism target.

DOI: 10.1002/stc

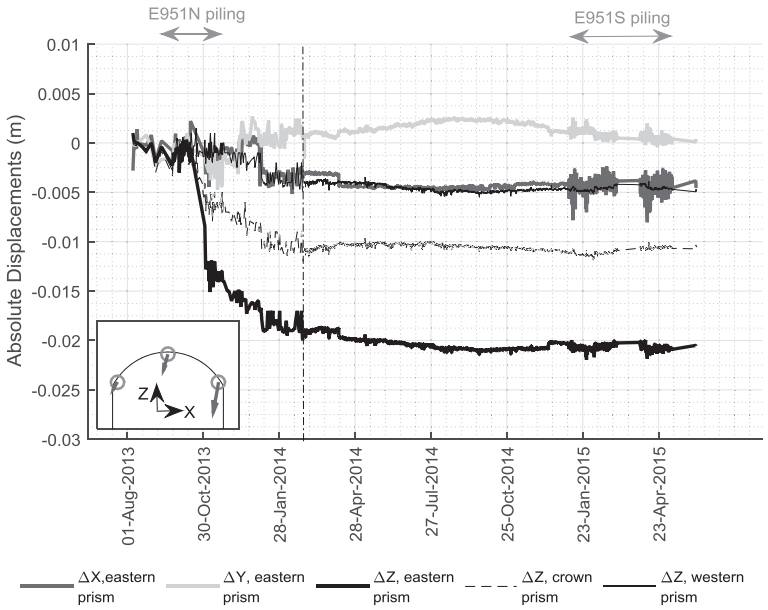

Figure 4. Absolute displacements of three station level targets along the highlighted longitudinal section of the arch between August 2013 and June 2015. An illustration of these displacements is shown in the inset (scaled by 100 times).

The elevation (Z-axis) data from the prisms show the expected settlements on the eastern side of the examined longitudinal section. A significant portion of these deformations were accumulated during the piling of E951N. When the construction of the piles was completed in E951N on 1 Nov 2013, movements of 13 mm had occurred. Gradual settlements caused further movements until early Jan 2014, where a total of 19-mm settlements was reached. The later phases of the construction and piling caused limited movements to bring the total settlement to 21 mm. A similar progression can be observed for the crown and western springing point prisms where most recent surveys indicate 11- and 4-mm reduction in elevation. Additionally, it is useful to explore the X and Y axes movement, which respectively describe the longitudinal and transverse actions. According to the total station data, consistent movements along the Y axis have not been observed. However, an approximately 5-mm movement was observed in the longitudinal X direction. It is interesting to note that a similar amount of longitudinal displacement is observed in all three prisms of the same longitudinal section. This is shown in the inset of Figure 4, where the arrows indicate the direction of movements. This figure demonstrates a rigid body translation of the arch in the longitudinal direction, which is unlikely. This measurement is likely due to accumulating errors in the control points.

The movement data in arch E951N are then used to calculate relevant engineering parameters, which are reported alongside the trigger levels for the alarms in Table I. First, the differential horizontal and vertical movement of the crowns of neighbouring arches are evaluated. Maximum differential horizontal movements are small, but the differential vertical movements were appreciable as minimal movement was observed in the neighbouring arches E950 and E952, where no significant construction work was carried out. These parameters concern the relative movements of arches, which relate to the serviceability of tracks. In addition, it is crucial to examine the serviceability of the load carrying

Table I. Engineering parameters derived from monitoring data from E951N and neighbouring arches.

	Green alarm*	Amber alarm*	Maximum measured
Differential horizontal movement (mm)	10	15	3.7
Differential vertical movement (mm)	15	25	19.3
Distortions	Figure 5	Figure 5	Figure 5

For each parameter, trigger thresholds for green and amber alarms are provided.
*The specified values specify the upper threshold of the respective alarms.

DOI: 10.1002/stc

arches. For this, a method that is typically used to describe the serviceability 'damage' of brick-bearing walls undergoing hogging settlements was adopted [8,11].

Boscardin and Cording's method [11] postulates that the damage observed in brick-bearing walls undergoing settlements can be correlated with the maximum observed tensile strains in the structure. In the original study, the wall is represented by a deep beam with an aspect ratio of 1:1, and the maximum tensile strain it experiences while undergoing hogging settlements is determined for a range of horizontal strains and angular distortions induced in the structure as a result of settlements. With little modification, this method was applied to masonry arches undergoing deformations during settlements. In this method, the horizontal strain ε_{hs} is defined as follows:

$$\varepsilon_{hs} = \frac{|\Delta_3 - \Delta_1|}{l} \tag{1}$$

where Δ_1, Δ_3 and l may refer to different variables. For the longitudinal axis of the arch, Δ_1 and Δ_3 describe the longitudinal movements at the springing points in the direction of X. Therefore, the horizontal strain describes the differential horizontal displacement of the arch normalized by the span l. For the transverse axis, Δ_1 and Δ_3 describe the transverse movements at the crown of the arch in the direction of Y. In this case, horizontal strain describes the differential horizontal movement at the arch along its transversal axis, normalized by the distance between two furthest crown prisms, which is again denoted by l.

The corresponding angular distortion β was defined as follows:

$$\beta = \frac{|2\Delta_{2z} - (\Delta_{1z} + \Delta_{3z})|}{l} \tag{2}$$

where Δ_{1z}, Δ_{2z} and Δ_{3z} describe the vertical movements observed at three target points along an axis. Consequently, for the longitudinal axis, β describes the relative angle of distortion of the crown with respect to the angle of distortion of the arch indicated by the springing points. Here, l denotes the longitudinal span. For the transversal axis, β describes the relative angle of distortion of the middle crown optical target from with respect to the distortion indicated by the other crown targets. Here, l denotes the distance between the crown targets furthest away.

The results of the calculations for horizontal strain and angular distortion are plotted in Figure 5. The damage levels for each trigger level were defined in [8] and relate to the definition that will be presented later in Table II. Despite the observed 20-mm settlements, almost no angular distortion is recorded in arch E951N. This is due to two reasons. First, the arch crown displacements are proportional to the relative vertical movements of the springing points (Figure 4). Consequently, according to Equation (2), there is negligible distortion in the arch in the longitudinal axis. Second, negligible distortion angles are recorded along the transversal axis, as the crown displacements do

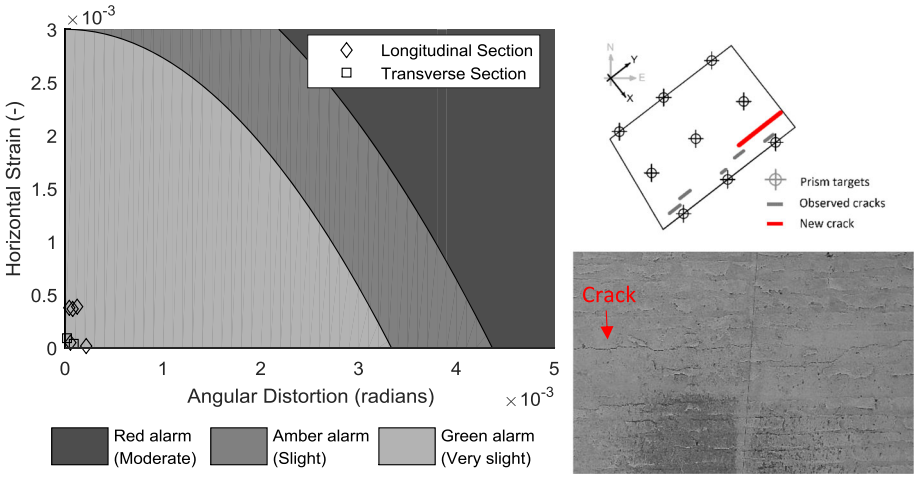

Figure 5. Damage assessment of E951N (left), location of cracks observed in the arch (right, top row) and a photo of the new crack that was observed after piling (right, bottom row).

DOI: 10.1002/stc

Table II. Guidelines for quantifying damage in low-rise masonry buildings [25].

Degree of damage	Description of typical damage (ease of repair)	Approximate crack width (mm)
Negligible	Hairline cracks of less than about 0.1-mm width are classified as negligible	Up to 0.1
Very slight	Fine cracks that can easily be treated during normal decoration. Perhaps isolated slight fracturing in building. Cracks rarely visible in external brickwork	Up to 1
Slight	Cracks easily filled. Re-decoration probably required. Recurrent cracks can be masked by suitable linings. Cracks not necessarily visible externally (some external repointing may be required to ensure weather tightness). Doors and windows may stick slightly	Up to 5

not vary significantly. Fractionally higher horizontal strains are observed; however, the data comfortably lie in the green alarm range.

From the use of these charts, it would appear that 20-mm settlements had negligible effects on the arch. However, upon closer inspection, a new transversal crack was observed alongside the existing cracks (Figure 5, right). While this crack did not negatively impact on the operation of the station, it is noteworthy that it was not spotted by the discussed damage assessment method. It is also important that Equation (2) calculated negligible distortions in the arch, despite considerable settlements. The aforementioned findings cast doubt on the suitability of this method for application to masonry arches.

In summary, the total station data proved useful while comparing the structural movements to predefined trigger limits. However, further information regarding the structural response of the arch is still necessary. Approximate methods attempt to quantify serviceability damage due to cracking, but they predict negligible distortion under 20 mm of settlement and do not agree well with visual observations. Distributed sensing by fibre optics and laser scanning aim to improve these aspects and are discussed in the next two sections.

4. DISTRIBUTED MONITORING USING FIBRE OPTICS

Instead of measuring the exact strain at a limited number of points, the method of BOTDR allows detection of strains, which are averaged for every metre. Averaged strain readings are provided with 5-cm intervals over the whole length of the optical fibre. Alongside its ability to sense distributed strains, the immunity of the sensing medium to several environmental effects offers new opportunities for long-term sensing [12,13]. Recently, the applications of fibre optics to large civil structures provided distributed strain information on a large scale, making critical assessment information accessible to engineers [14–20]. Additionally, a significant body of work has focused on quantifying the accuracy of fibre optics in crack detection [21–23]. These works highlight the sub-millimetric accuracy of fibres in movement detection.

The use of BOTDR has been limited for masonry structures [17,24]. The existing studies have utilized BOTDR to quantify the change of load paths. Another possible use for BOTDR data is monitoring the long-term movement of existing cracks and tracking the formation of new cracks in the instrumented face of the structure. This can be particularly useful as visible cracking has been a traditional indicator of damage in masonry. In particular, the Building Research Establishment guidelines [25] provide assessment tables that correlate crack opening due to settlements (amongst other parameters) with a number of damage states (Table II).

In this project, arch E951N was instrumented with optical fibres before the piling works commenced. To attach fibres to the masonry surface, a ‘hook and pulley’ method was utilized (Figure 6, left). First, holes were drilled into brick masonry and a hook was fixed with a wall plug. Then a pulley was slotted onto the hook, fixing it in place with a structural adhesive. To obtain estimates of true movements between hooks, the distance between hooks needed to exceed the spatial resolution of the fibre optics analyser. Therefore, hooks were placed at approximately 2 m away from one another.

DOI: 10.1002/stc

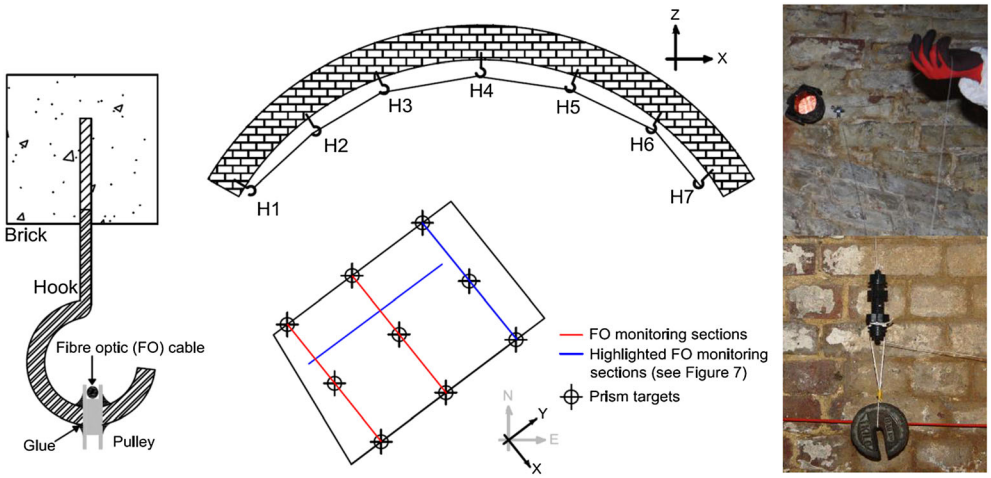

Figure 6. Illustrations of the attachment of fibre optic cables to masonry (left), arrangement of fibres in the arch (middle) and photos describing the installation (right).

For the longitudinal sections, this meant that the relative axial movements between seven hooks, H1–H7, could be determined (Figure 6, top row, middle). After the hook and pulley assemblies of a given section were in place, the single mode Hitachi fibre was placed on the pulley slot on which it was free to slide. It was then necessary to pretension the fibre to detect compressive strains. This was achieved by placing weights on either end of the longitudinal monitoring section. Plastic clamps gripped on to a small stretch of fibre while the weights were attached to these clamps (Figure 6, bottom row, right). After checking that all the sections were in tension, structural adhesives were used to glue the cables to the hook.

The spatial arrangement of the fibres followed the layout of the optical targets. Figure 6 (bottom row, middle) shows the three longitudinal sections of the fibres and a single transverse section in the plan view of arch E951N. After laying out all the sections, an extension cable was spliced to the strain sensing Hitachi cable and routed to an enclosed cross-passage between E951S and E952, where monitoring was carried out. Yokogawa AQ 8603 analyser was used to perform BOTDR measurements bi-weekly. According to the manufacturer, the device is accurate to $\pm 40\mu\varepsilon$ (accuracy is defined as two standard deviations with the unit of microstrain [26]). The analyser determines the characteristics of reflected light (i.e. central frequency of the Brillouin gain spectrum). The changes in reflected light characteristics over time are linearly proportional to the changes in strain and temperature of the fibre. After compensating for temperature changes, using the slack sections of the fibre, the mechanical strain is determined (e.g. see [17] for further details).

Figure 7 (top row) shows the normalized and uncompensated total strain data for the first hundred metres of the cable. Four readings that followed the baseline reading on 13 Sept 13 are shown. The last reading was taken on 11 Nov 13, after the last pile was constructed in arch E951N on 1 Nov 13. Further readings could not be taken as the fibres were damaged. Therefore, the results do not indicate the final state of the arch, but according to total station data (Figure 4), considerable movements (around 13-mm settlement) had occurred by 11 Nov 13.

Figure 7 (top row) illustrates the cable route from the analyser to the extension cables and to the transverse and longitudinal sections of E951N. Next, the temperature compensated data are shown for the highlighted fibre optic monitoring sections (Figure 6, bottom row, middle). Tension is shown as positive while compression is shown as negative. The mechanical strains observed in the transverse section fibres indicate strains that are smaller than $100\mu\varepsilon$ in magnitude, which corresponds to fluctuations that were observed in consecutive readings taken during a given day. For the 2-m gauge length, these readings suggest less than 0.2-mm transverse movements. Therefore, in agreement with the total station data, no significant transverse movement is observed. The axial mechanical strain change in the northernmost longitudinal section is presented next. The precise location of hooks H3–H7 is highlighted in the inset. Here, a significant peak in tension for the final data set from 11 Nov 13 is observed. In comparison with other compressive and tensile stresses observed in the section, the strains

DOI: 10.1002/stc

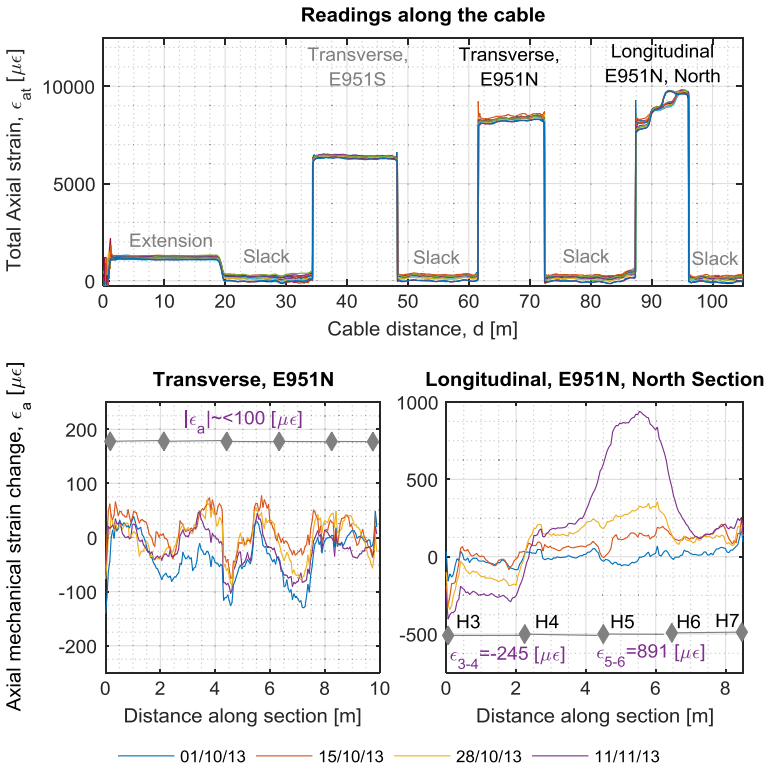

Figure 7. Normalized total axial strains along the first 100 m of the fibre (top row) and changes in axial mechanical axial strain during piling for highlighted cross sections (bottom row).

are high in magnitude. Using the truncated averaging method, which averages the strain readings from locations, which are only affected by the uniform strain in that stretch of the cable [27], the true strain can be calculated. These are reported in the figure for sections between hooks 3 and 4, and 5 and 6, as $-245\mu\varepsilon$ and $891\mu\varepsilon$.

Making inferences from the strain data requires assumptions regarding the particular mode of load carrying mechanism of the structure. As a simple and conservative approach, limit analysis assumptions may be utilized [28]. These assumptions are as follows: (i) masonry does not exhibit sliding, and (ii) it has infinite compressive strength and zero tensile strength. As a result, the loads are transferred through the structure via a thrust line. Initially, as there are no visible signs of cracking, and it may be assumed that the thrust line lies inside the arch. However, to sustain support movements, thrust line migrates to the intrados and extrados of the arch, forming hinges. These hinges provide rotational releases, leading to a kinematic mechanism, where assemblies of rigid bodies rotate with respect to one another.

According to these assumptions, the intrados tensile strains are wholly due to hinge formations at the extrados of the arch, causing crack openings on the intrados. This would suggest a crack opening of 1.8 mm by multiplying the true strain and the exact gauge length of the section H5–H6. This is a conservative estimate; the tensile strength provided by mortar and the migration of initial compressive stresses present in the intrados are neglected. In addition, owing to the 2-m gauge length adopted for the fixing points, the hinge rotations may have resulted in overestimating crack openings. However, the detection of a 2.5-mm crack in the location indicated by the fibre optics after piling (Figure 5) is consistent with this interpretation.

A similar discussion is necessary for evaluating the recorded compressive strains. In the sections shown in Figure 7 (bottom row, right) and other longitudinal sections, the compressive strains do not exceed $500\mu\varepsilon$ in magnitude. This is due to the fact that for compressive hinges on the intrados, the large movements due to hinge rotations would be concentrated on the crack opening at the extrados. The recorded compressive strains are due to the migration of the thrust line towards the intrados. As a result, it is difficult to ascertain the existence of compressive hinge locations from the

DOI: 10.1002/stc

data. However, the results suggest a concentration of compressive forces in the crown and towards the western springing point.

In summary, this section described the installation, and the data gathered from the distributed fibre optic sensor system deployed on a masonry vault. The strain sensing fibre optic data provide information on the changing load paths in the structure. This information is valuable for calibrating finite element models, where only rough estimates for masonry elasticity are available (Section 6). More importantly, the data provide an approximate indication of intrados crack opening. On the basis of these results, it is concluded that the distributed fibre optic sensor systems provide a new opportunity to sense crack locations and widths in masonry without previous knowledge of where they will appear. However, to interpret these relative strain results, a global understanding of displacements is necessary. This is examined in the next section.

5. DISTRIBUTED MONITORING USING LASER SCANNERS

Terrestrial laser scanners are geomatic devices equipped with a laser beam and precise servomotors. They collect 3D point data and can carry out similar surveying operations to total stations. While they are not commonly used in the structural health monitoring field, several pioneering studies have demonstrated their potential [6,29–33].

To compare different point clouds is challenging. In particular, registering clouds to the same coordinate system accurately is critical, as slight errors in registration may render further comparisons unreliable [34]. In this project, instead of using automatic registration techniques, robust surveying registration techniques were used. The survey grid coordinates of optical targets (which are recognized by laser scans) were used for a resection-based registration and georeferencing. In all instances, successful registrations were achieved to the survey grid with errors smaller than single-point measurement accuracies.

Computing displacement fields from feature-less clouds is another challenge. Currently, the existing approaches to comparing point clouds can be grouped under two headings. The first approach computes distances between clouds. Existing methods include the determination of the closest point-to-point distance between two point clouds (e.g. [29]). Recently, Lague *et al*. [35] improved these techniques with a new method called Multiscale Model to Model Cloud Comparison (M3C2), where local plane fits to the cloud reduce measurement noise errors and allow determination of the distance between clouds in predefined directions (Figure 8, left). The second approach is the computation of displacement vectors on the basis of identifying corresponding sections of two point clouds. These methods determine the rigid body roto-translation matrix of the displaced object between two scans. The Teza *et al*. piecewise alignment method (PAM) [36], uses the Iterative Closest Point algorithm to compute this matrix (Figure 8, right). In this method, the distances between the corresponding object in two clouds are minimized with an optimization algorithm, starting with an initial guess based on the closest distance between clouds. Both of these methods are used in this study to explore the settlement response of arch E951N.

Figure 9 (left) shows a laser scanner during operation. The first scan was carried out shortly before the piling works. In this instance, the phase-based FARO Focus 3D S20 laser scanner was used to take high-resolution scans from the northern part of E951N (Figure 9, bottom middle). This scanner

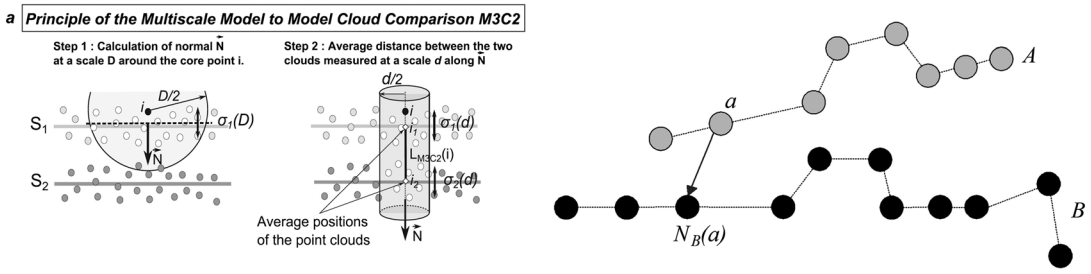

Figure 8. Methods for comparing laser scan point clouds: M3C2 method (left) [35] and PAM (right) [36].

DOI: 10.1002/stc

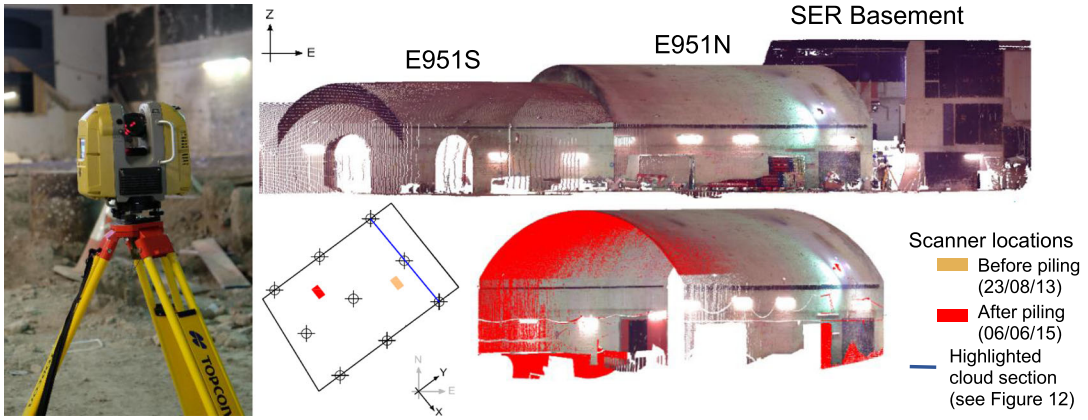

Figure 9. A laser scanner in operation (left), a colorized point cloud (top right) and illustrations of the scanner locations and cleaned point clouds from laser scan surveys before and after piling (bottom right).

provides measurements within a 20-m radius with a ranging error of 2 mm (defined as a standard deviation of values about the best-fit plane) and angle measurement error of 32 arc sec. Registration and georeferencing were achieved with the use of four spherical targets that are recognized by the SCENE (version 5.5.0, Lake Mary, FL, USA) software during post-processing. The coordinates of these targets were determined by manual total station monitoring and were used for georeferencing. Later, for the scan after piling, the long-range (0–150 m) time of flight laser scanner Topcon GLS-2000 was used. This scanner provides measurements with a ranging error of 2 mm (defined as above) and angle measurement error of 6 arc sec. With this scanner, target registration was achieved with the scanning of the existing optical prism targets (Figure 3). In order to detect these optical targets, scanning was carried out on the southwestern portion of the arch. The coordinates of these optical targets were retrieved from the automatic total stations and were used for registration and georeferencing using the SCANMASTER (Version 3.0.3, Tokyo, Japan) software. A registration that recorded a maximum error of 2 mm was achieved using six optical targets.

After registration, the laser scan data are pre-processed for comparisons using the open software CLOUD COMPARE (Version 2.6.2, Clamart, France). First, the unnecessary data are eliminated. This manual process resulted in the elimination of some useful point data (e.g. the eastern pier wall was partially occluded owing to reinforcement bars of the vaults; see Figure 2, top right). As a result, comparisons could not be carried out in some regions. After the initial pre-processing, the data were segmented into the construction joint walls, pier walls and the vault. This was achieved using edge detection tools, which helped locate the intersection of two surfaces with different curvatures. Later, using the identified edges, longitudinal and transverse section cuts of the cloud could be made for detailed analysis.

Figures 10 and 11 show the comparison of the vault and western pier wall clouds using the M3C2 method with a normal scale of 2.5 cm [39]. These M3C2 comparisons assess respectively the vertical distances and along normal horizontal distances between clouds. In particular, Figure 10 highlights the vertical settlements that are experienced on the eastern side of the vault owing to piling, in the range of −20 to −30 mm. In contrast, settlements are smaller than −5 mm towards the western pier. Here, some displacements indicate a surprising increase in elevation up to 5 mm on the northern end. In general, an increasing trend in settlements towards the south can be observed.

Figure 11 shows the corresponding horizontal movements detected by the M3C2 along the local normal directions of the western pier (in the direction of X). The movements are appreciably smaller in the south, around −5 mm, and significantly higher in the north, close to −10 mm. It is important to indicate that on the visible northern section of the eastern pier where analyses were carried out (Figure 9), a corresponding movement of −7 mm in direction of X can also be observed. This was accompanied by a similar movement on the eastern pier wall, indicating a lateral rigid body movement of the arch. In Section 3, the total station data indicated a similar rigid body movement of the arch of −3 mm in the direction of X (Figure 4). It was discussed that this movement may have arisen owing to changes experienced in the control points. It is evident from Figure 11 that these errors also affected the registration and their effects on M3C2 measurements are discussed next.

DOI: 10.1002/stc

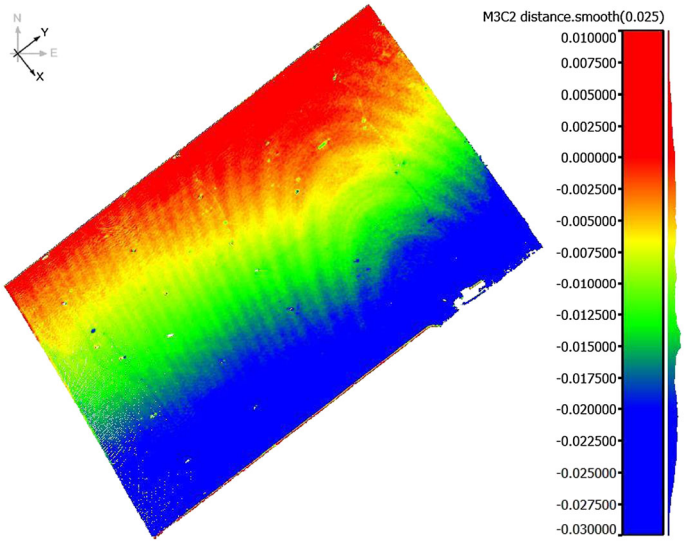

Figure 10. Vertical displacement of the vault of arch E951N estimated by the M3C2 method.

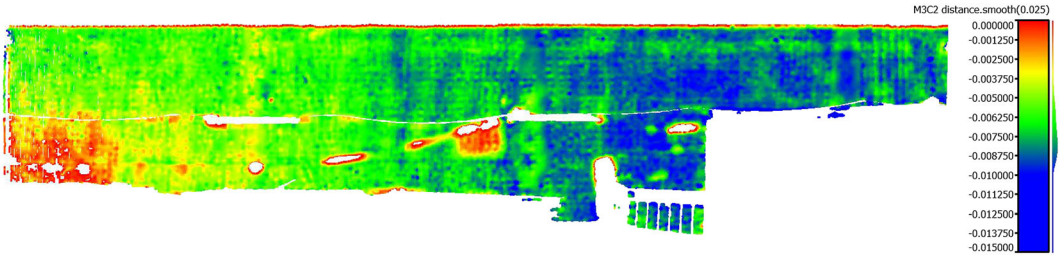

Figure 11. Horizontal displacement of the western pier of arch E951N estimated by the M3C2 method.

Figure 12 shows the vertical displacement estimates for locations along the longitudinal axis of the arch using a section cut (see the highlighted cloud section specified in Figure 9). There is significant noise in the raw data owing to the process of fitting horizontal planes to a curved surface. The fluctuations approach 10 mm close to the springing points but decrease considerably at the crown, where the arch is flattest, to around 1 mm. These noisy data were filtered with Savitzky–Golay filters to reveal a clear pattern of displacements, which again highlighted the increase in elevation on the northwestern side of the vault. The reason for the increase in elevations is explained by a schematic (inset in Figure 12). Owing to the rigid body movement of the coordinate system, a significant change is observed in the vertical distances between the clouds. This is due to the curved surface of the arch, where small lateral rigid body movements can cause significant distance differentials in the vertical direction. To correct for these cloud migration errors, the after-piling section cloud is translated 7 mm in the direction of X. After this compensation, the measurements now report smaller settlements close to the western and eastern springing points, while the indicated crown settlements do not significantly change.

The PAM [36] was also applied to the same longitudinal section of the cloud. To apply the PAM, the georeferenced 'after piling' cloud section was segmented into ten subsections of equal width. Then, using the Iterative Closest Point algorithm without subsampling the cloud, these subsections were registered to the 'before piling' cloud, and the movements were recorded. These movements are illustrated in Figure 13 for the longitudinal direction, as the transverse movements were negligible. A good agreement can be observed from the data where both total stations and PAM show the rigid body lateral movement and vertical settlements of the arch. However, the PAM appears to underestimate the vertical movements close to the springing points. These errors are due to the inherent difficulty in spotting unique correspondences between the clouds on the basis of the simple geometry

DOI: 10.1002/stc

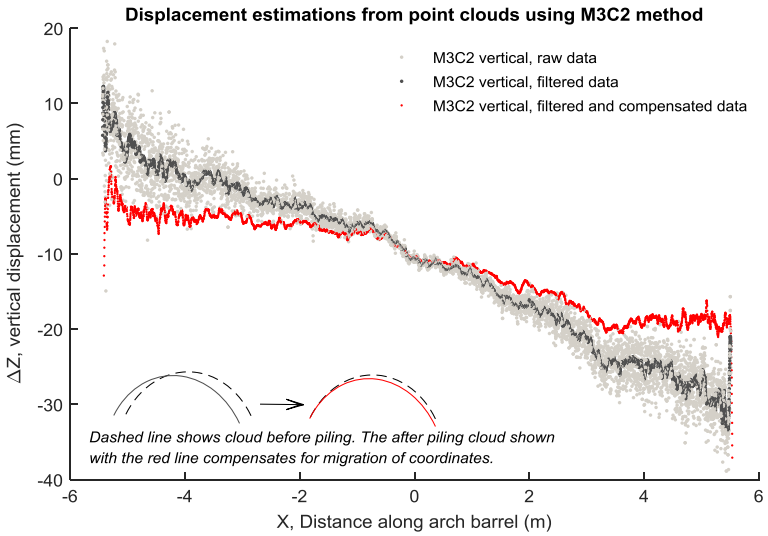

Figure 12. Vertical movement of the highlighted longitudinal section in E951N estimated by the M3C2 method, before and after filtering and compensation.

of the arches. Despite this shortcoming, it is noteworthy that the PAM is not significantly affected by cloud migration errors.

Figure 14 compares the accuracy of the vertical displacements estimated by the M3C2 and PAM against the total station data. The raw M3C2 data are not precise, but when the data are filtered and compensated, it yields accurate estimates for vertical movements. The results are within 3 mm of the total station results and capture the structural response in significant detail. The PAM yields good movement estimates for the crown of the arch, but it underestimates vertical movements close to the western and eastern springing points. However, improved PAM estimations may be possible if denser clouds from closer scanning positions are used [36], where mortar joints are captured. Nonetheless, both cloud comparison reveal comprehensive information on the global structural response.

6. STRUCTURAL EVALUATION USING DISTRIBUTED MONITORING DATA

Mathematical modelling enables a better understanding of the structural behaviour and allows to predict the structural response to specific actions. In the specific case of masonry arches, the biggest

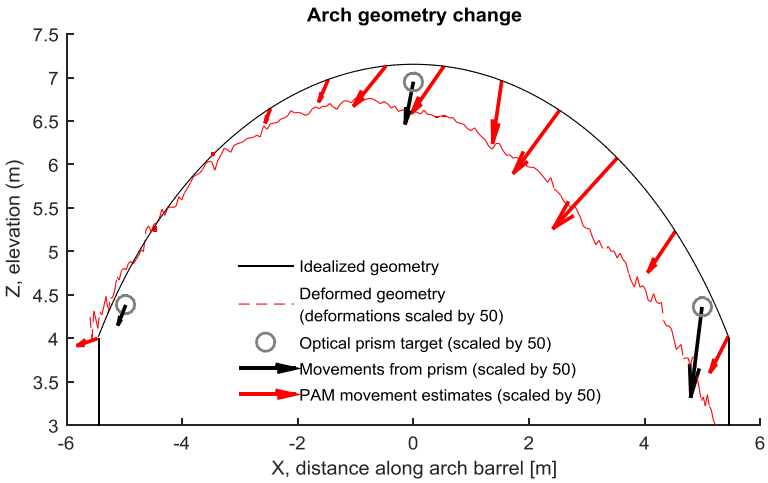

Figure 13. Movements of the highlighted longitudinal section in E951N estimated by the PAM.

DOI: 10.1002/stc

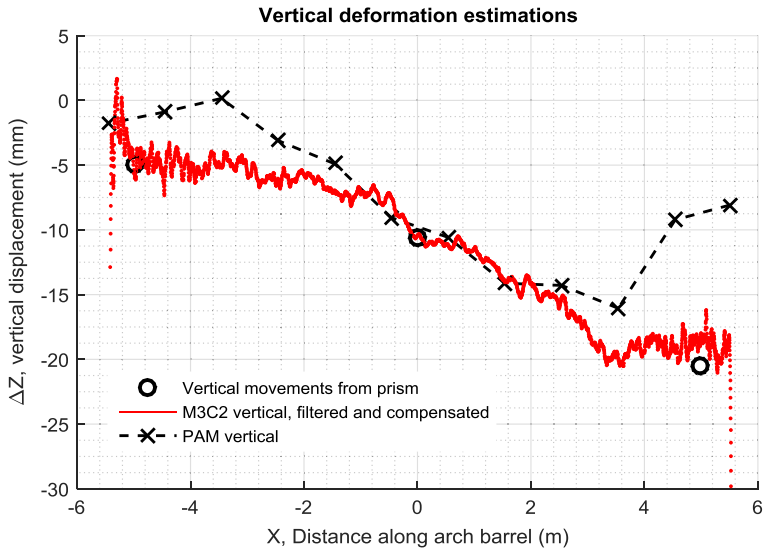

Figure 14. Comparison of vertical deformations estimated from total stations and cloud comparison techniques M3C2 and PAM.

modelling challenge relates to the uncertainties associated to materials and boundary conditions [2]. The distributed data presented in Sections 4 and 5 provide the opportunity to assess modelling assumptions and therefore to validate analytical and computational models.

In this study, two approaches are used to simulate the response of the masonry arch to settlements. The first one is the mechanism method. This method utilizes the limit state assumptions (Section 4). Admissible kinematic mechanisms are determined for describing the settlement response of the arch, and through an optimization process, the mechanism that minimizes the external work carried out by support forces is determined. The second approach is modelling masonry by a homogenous continuum and utilizing the finite element method. Here, additional aspects such as the elasticity of masonry can be included in the response. These analyses were performed using LIMITSTATE RING (Version 3.1, Sheffield, UK) and DIANA (version 9.6, Delft, Netherlands) software, respectively.

The same longitudinal section that was examined in Sections 3, 4 and 5 was modelled. The mechanism model was created by using the geometry defined in Figure 2. The finite element model was constructed by discretizing the same geometry into a dense quadratic mesh (Figure 15). The brickwork and fill were modelled by eight-node plane stress elements with a 3×3 point Gaussian integration scheme. The choice of plane stress elements is justified by the closeness of the section to the northern edge of the vault where the movement in the transverse direction is not restrained. However, the plane stress assumption does not affect the results and yields near identical results to plane strain analyses (not shown). A coaxial rotating crack model was used with a linear tension softening relation after cracking for the brickwork. The model provides crack strains, which have to be translated to crack widths via the use of the crack bandwidth as a finite element discretization

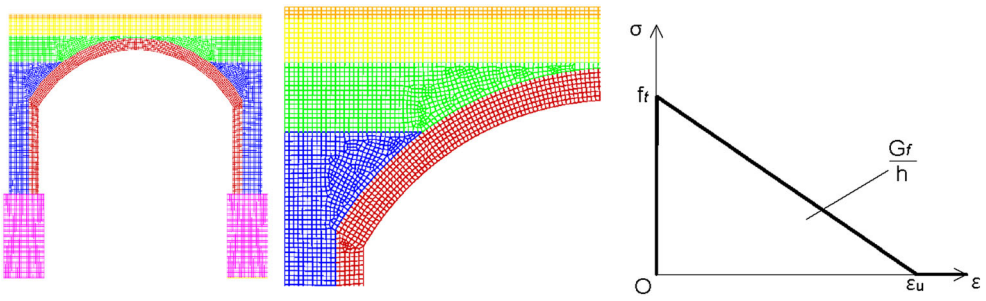

Figure 15. A schematic of the finite element model showing the geometry (left), mesh detail (middle) and the linear softening relation adopted for the rotating crack model (right).

DOI: 10.1002/stc

parameter [37]. The maximum crack width has been derived by multiplying h by the maximum crack strain value. The tension softening law (Figure 15) was defined by the tensile strength f_t, the fracture energy G_f and the crack bandwidth h, which is related to the element size and equal to 100 mm. By using the coaxial rotating crack model, the structure is modelled as a homogeneous isotropic linear elastic continuum before cracking, while it behaves as a non-linear orthotropic continuum after the crack onset. A linear elastic material model was utilized to describe the contribution of the fill to the response. A frictional interface was defined between the lime concrete fill and the load carrying arch. In addition, rollers that are free to slide in the vertical direction were defined along the edge of the piers from the springing point up, to simulate the existing boundary conditions imposed by the adjacent

Table III. Values for various parameters used for mathematical modelling.

	Reference value	Value range
(i) Mechanism models		
Small lateral movements (mm)	0	−5, 5
Lime concrete fill cohesion, c_f (kPa)	200	0, 400
Lime concrete fill friction angle, φ (degrees)	35	0, 40
Ring debonding	None	None, complete
(ii) Finite element models		
Young's modulus of brickwork, E (kPa)	2.2e+6	1.1e+6, 4.4e+6
Tensile strength of brickwork, f_t (kPa)	0.1e+3	0.05e+3, 0.2e+3
Fracture strength of brickwork, G_f (N/mm)	0.005	0.0025, 0.01
Young's modulus of lime concrete fill (kPa)	2200	220, 2200
Backfill – arch interface tensile stiffness (N/mm)	100	No interface, frictional interface
Backfill – arch interface shear stiffness (N/mm)	0.1	Not examined
Backfill – arch interface cohesion (kPa)	1400	Not examined
Backfill – arch interface friction angle, φ (degrees)	35	Not examined

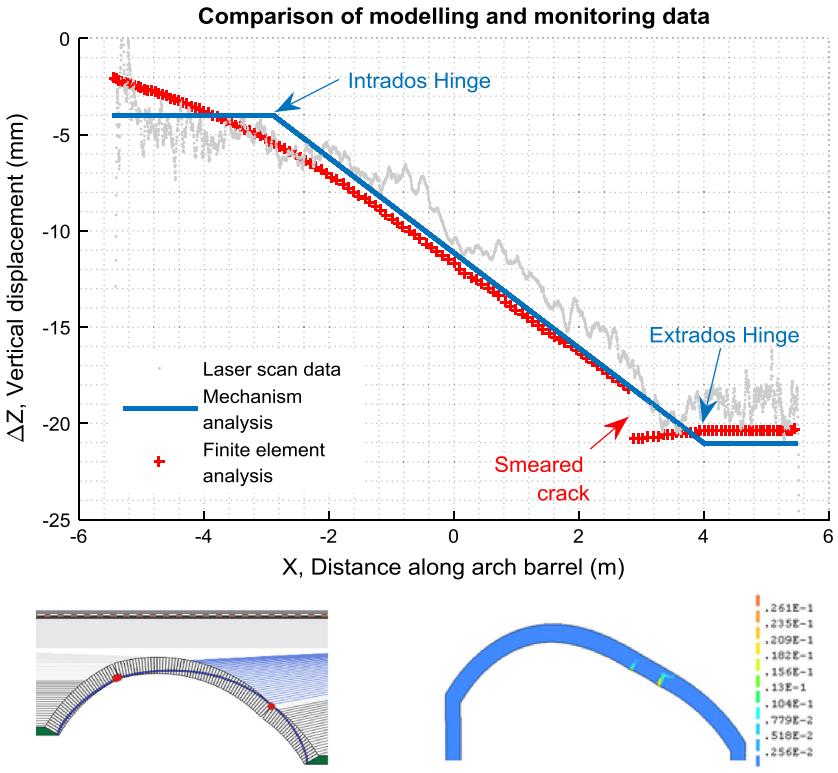

Figure 16. Comparison of vertical deformations estimated from the M3C2 method, mechanism and finite element models. (top), presented with the deformed shapes from the mechanism model (left) and finite element model (right), where the contour colour plot on the deformed shape shows the principal strain values.

DOI: 10.1002/stc

arches. Line interface elements with no tensile strength were defined at the foundation–structure interface, in order to apply the gradual settlement effects. Vertical settlements of 13 and 20 mm were applied to the models to compare the results with fibre optics and laser scanning results, respectively (Sections 3 and 4).

A number of assumptions were required during the modelling process for defining material characteristics. Therefore, a large range of values were examined to investigate the model sensitivity to these parameters. Parameters and values are summarized in Table III. The reference parameters were determined using existing material tests [3], Network Rail codes practice (NR-GN-CIV-025) and Eurocodes (EC6). Where an estimate could not be made, such as for tensile strength and fracture energy, conventional values from previous studies (e.g. [38,39]) were adopted.

Monitored and simulated vertical movements of the arch are compared in Figure 16. The mechanism model indicates the development of two hinges roughly at the same height. The vertical displacement profile between these hinges is linear. The deformation of the finite element model is qualitatively similar, and the localization of the tensile principal stresses indicates intrados cracks at similar locations. Simulated total crack width (1 mm) is similar to the value measured by the fibre optics (1.8 mm).

As indicated previously in Table III, a range of modelling assumptions and parameters were investigated. Some of these aspects are discussed in Figure 17 as they help to understand the factors governing the arch response. The first row shows the parametric analyses carried out using the mechanism analysis models. Owing to the uncertainty regarding the lateral displacements experienced during piling (Section 3), the effect of lateral support movements on arch response was explored. These lateral movements caused significant changes in the arch response mechanism, which did not agree with the observed results. Therefore, the assumption of negligible lateral movement was verified. Then, the effects of ring delamination and soil pressure were examined. The arch was originally modelled as a well-bonded brick assembly as inspections did not reveal any visible presence of ring delamination.

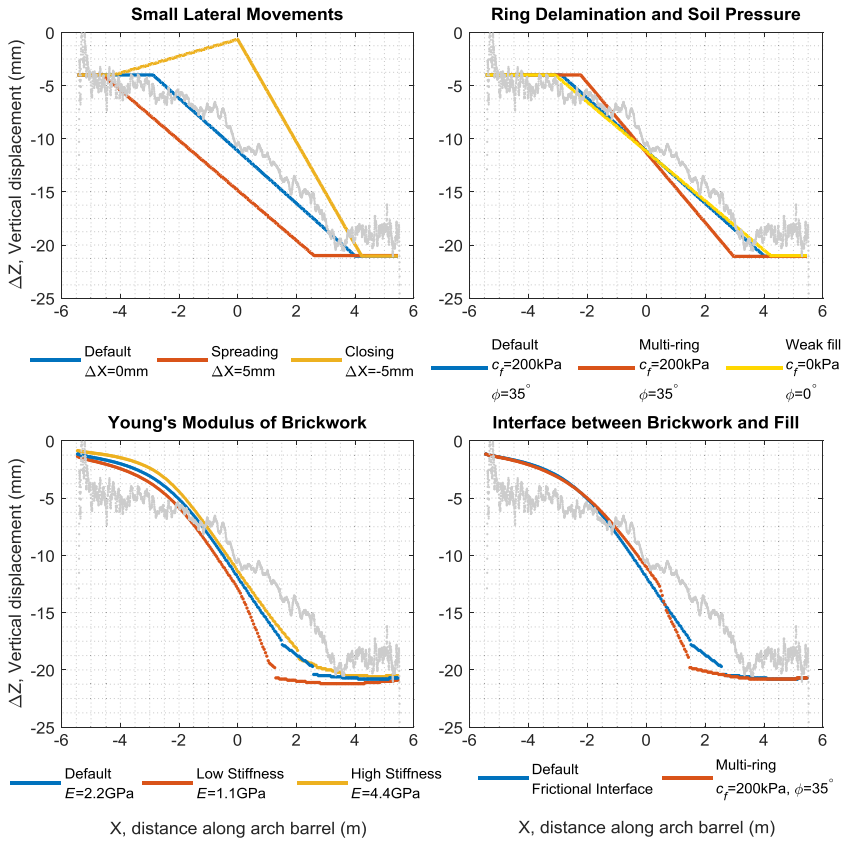

Figure 17. Comparison of the effect of several modelling assumptions on the vertical displacement response using mechanism (top row) and finite element models (bottom row).

DOI: 10.1002/stc

However, the analyses indicate that a similar intrados settlement profile would be observed even if the rings had separated. The overall global response of the arch would of course be different and ring separation would have important implications on arch settlement and load capacities. However, in the absence of conclusive evidence, it was assumed that ring separation did not occur. The investigation of the cohesion and angle of friction of the backfill was also necessary as there were uncertainties regarding the material characteristics of the lime concrete fill. It is observed that the choice of material cohesion and angle of friction does not have significant bearing on the response.

On the basis of these findings, detailed finite element model sensitivity analyses followed. These analyses first investigated the effects of elasticity modulus and cracking model parameters of brickwork. A variation in the Young's modulus (Figure 17, bottom left) leads to a modified global stiffness of the arch, which exhibits larger vertical movements for lower values of Young's modulus. However, the reference parameter (see Table III) provides the best agreement with the intrados strain distribution measured by fibre optic sensors. Furthermore, a reduction in the tensile strength causes an earlier cracking of the structure, while a reduction in fracture energy results in a more brittle response. Finally, an investigation of backfill–arch interface properties was made (Figure 17, bottom right). Modelling the backfill–arch interface with low tensile strength and frictional shear behaviour provides the degree of freedom required for arch movement. Otherwise, when modelled as a continuum, the tensile stresses applied by the stiff backfill on the masonry arch distort the settlement profile.

Overall, the analyses from Figure 17 demonstrate how the distributed sensing data from fibre optics and laser scanning enable a deeper understanding of structural response and the formulation of more accurate modelling strategies.

7. CONCLUSIONS

This study discussed the monitoring data from a masonry vault undergoing settlements during nearby piling. The data were gathered by three different sensor systems: total stations, fibre optics and laser scanning. The discussions focused on the use of monitoring data for obtaining (i) a better understanding of the movements of the structure, (ii) a better appreciation of the damage sustained by the structure and (iii) an evaluation of the structural response through comparison with analytical and computational modelling results. These discussions were informed by the relative accuracy and precision of the monitoring data.

In summary, the total stations provide the most precise movement information, yet their limited spatial coverage makes it difficult to utilize them for evaluations of damage and structural response. In contrast, distributed sensors provide significantly higher spatial coverage, and this makes them better suited for monitoring the discrete behaviour of masonry. Distributed fibre optic strain system yields useful estimates for the location and width of new radial cracks that formed during piling. This unique capability is useful for serviceability-based damage assessment. Laser scanners gather point cloud data, which are used to determine vertical movements at all visible points on the arch. The M3C2 method resulted in vertical movement estimates of high accuracy but low precision, whereas the PAM described movements in three dimensions but with decreased accuracy. Together, the distributed data enabled calibration of finite element models. The calibration highlighted the important components of response and enables further investigations as it better quantifies the damage state of the arch after piling.

ACKNOWLEDGEMENTS

The work carried out was funded by EPSRC and Innovate UK, through the Cambridge Centre for Smart Infrastructure and Construction (Grant Reference Number EP/L010917/1). The research materials supporting this publication can be accessed at https://www.repository.cam.ac.uk/handle/1810/254826. The authors are grateful to Tim Embley of Costain and Jim Woodhams of Topcon for making this project possible. Help from a number of individuals requires special mention; Vincent Auzel of Soldata, Dean Bain of Costain and Andy Evans of Topcon provided useful information that enabled this study. CSIC colleagues Peter Knott, Jason Shardelow and Emanuele Giglio assisted in site work, and discussions with Matthew DeJong helped improve the manuscript.

DOI: 10.1002/stc

REFERENCES

1. Hyder-WSP. Arch settlement assessment report – Arches E929, E930 & E951. Report No. N420-COT-REP-GO-000008. London, 2015.
2. Lourenço PB. Computations on historic masonry structures. *Progress in Structural Engineering and Materials* 2002; **4**(3): 301–319.
3. Alan Baxter Associates. London Bridge station structural investigations: interpretative report. Report No. N231-32112-ALB-REP-ST-000027. London, 2011.
4. Alan Baxter Associates. London Bridge station historical study. Report No. N231-104733-ALB-REP-ST-00001. London, 2009.
5. Psimoulis PA, Stiros SC. Measurement of deflections and of oscillation frequencies of engineering structures using robotic theodolites (RTS). *Engineering Structures* 2007; **29**(12):3312–3324.
6. Soni A, Robson S, Gleeson B. Structural monitoring for the rail industry using conventional survey, laser scanning and photogrammetry. *Applied Geomatics* 2015; **7**(2):123–138.
7. Hyder-WSP. London Bridge station redevelopment advanced monitoring specification. Report No. N420-COT-ESP-CS-000003. London, 2012.
8. Richmond J, Parker J, Sharratt M. The Shard, London, UK: response of arches to ground movements. *Proceedings of the ICE – Bridge Engineering* 2012; **165**(3):185–194.
9. Leica Geosystems. Leica Viva TS15. (Available from: http://www.leica-geosystems.co.uk/downloads123/zz/tps/VivaTS15/brochures-datasheet/LeicaVivaTS15Datasheet_en.pdf) [accessed September 30, 2015].
10. Leica Geosystems. Leica Nova TS50. (Available from: http://www.leica-geosystems.co.uk/downloads123/zz/tps/nova_ts50/brochures-datasheet/Leica_Nova_TS50_DAT_en.pdf) [accessed September 30, 2015].
11. Boscardin MD, Cording EJ. Building response to excavation induced settlement. *Journal of Geotechnical Engineering* 1989; **115**(1):1–21.
12. Nikles M, Thevenaz L, Robert PA. Simple distributed fiber sensor based on Brillouin gain spectrum analysis. *Optics Letters* 1996; **21**(10):758.
13. DeMerchant M, Brown A, Bao X, Bremner T. Structural monitoring by use of a Brillouin distributed sensor. *Applied Optics* 1999; **38**(13):2755–2759.
14. Klar A, Bennett PJ, Soga K, Mair RJ, Tester P, Fernie R, *et al.* Distributed strain measurement for pile foundations. *Proceedings of the ICE – Geotechnical Engineering* 2006; **159**(3):135–144.
15. Mohamad H, Soga K, Pellew A, Bennett PJ. Performance monitoring of a secant-piled wall using distributed fiber optic strain sensing. *Journal of Geotechnical and Geoenvironmental Engineering* 2011; **137**(12):1236–1243.
16. Matta F, Bastianini F, Galati N, Casadei P, Nanni A. Distributed strain measurement in steel bridge with fiber optic sensors: validation through diagnostic load test. *journal of Performance of Constructed Facilities* 2008; **22**(4):264–273.
17. Mohamad H, Bennett PJ, Soga K, Mair RJ, Bowers K. Behaviour of an old masonry tunnel due to tunnelling-induced ground settlement. *Geotechnique* 2010; **60**(12):927–938.
18. Glisic B, Yao Y. Fiber optic method for health assessment of pipelines subjected to earthquake-induced ground movement. *Structural Health Monitoring* 2012; **11**(6):696–711.
19. Schwamb T, Soga K, Mair RJ, Elshafie MZEB, Sutherden R, Boquet C, *et al.* Fibre optic monitoring of a deep circular excavation. *Proceedings of the ICE – Geotechnical Engineering* 2014; **167**(2):144–154.
20. Regier R, Hoult NA. Distributed strain behavior of a reinforced concrete bridge: case study. *Journal of Bridge Engineering* 2014; **19**(12):1–9.
21. Zhang H, Wu Z. Performance evaluation of BOTDR-based distributed fiber optic sensors for crack monitoring. *Structural Health Monitoring* 2008; **7**(2):143–156.
22. Ravet F, Briffod F, Glisić B, Nikles̀ M, Inaudi D. Submillimeter crack detection with Brillouin-based fiber-optic sensors. *IEEE Sensors Journal* 2009; **9**(11):1391–1396.
23. Feng X, Zhou J, Sun C, Zhang X, Ansari F. Theoretical and experimental investigations into crack detection with BOTDR-distributed fiber optic sensors. *Journal of Engineering Mechanics* 2013; **139**(12):1797–1807.
24. Bastianini F, Corradi M, Borri A, di Tommaso A. Retrofit and monitoring of an historical building using "smart" CFRP with embedded fibre optic Brillouin sensors. *Construction and Building Materials* 2005; **19**(7):525–535.
25. UK Building Research Establishment Digest. Assessment of damage in low-rise buildings with particular reference to progressive foundation movement, 1981.
26. Yokogawa Electric Cooperation. Yokogawa AQ8603. 2005. (Available from: http://tmi.yokogawa.com/files/uploaded/buaq8603_00e_1.pdf) [accessed October 1, 2015].
27. Iten M. Novel Applications of Distributed Fiber Optic Sensing in Geotechnical Engineering. ETH Zurich: Zurich, Switzerland, 2011.
28. Heyman J. The stone skeleton. *International Journal of Solids and Structures* 1966; **2**(2):249–279.
29. Girardeau-Montaut D, Roux M. Change detection on points cloud data acquired with a ground laser scanner. International Archives of Photogrammetry, Remote Sensing and Spatial Information Sciences, 2005.
30. Olsen MJ, Kuester F, Chang BJ, Hutchinson TC. Terrestrial laser scanning-based structural damage assessment. *Journal of Computing in Civil Engineering* 2010; **24**(3):264–272.
31. Nuttens T, Stal C, De Backer H, Schotte K, Van Bogaert P, De Wulf A. Methodology for the ovalization monitoring of newly built circular train tunnels based on laser scanning: Liefkenshoek Rail Link (Belgium). *Automation in Construction* 2014; **43**:1–9.
32. Mosalam KM, Takhirov SM, Park S. Applications of laser scanning to structures in laboratory tests and field. *Structural Control and Health Monitoring* 2014; **21**(1):115–134.
33. Lindenbergh R, Pietrzyk P. Change detection and deformation analysis using static and mobile laser scanning. *Applied Geomatics* 2015; **7**(2):65–74.
34. Van Genechten B, Demeyere T, Herinckx S, Goos J, Schueremans L, Roose D, *et al*. Terrestrial laser scanning in architectural heritage – deformation analysis and the automatic generation of 2D cross-sections. 22nd CIPA Symposium, Kyoto, 2009.

DOI: 10.1002/stc

35. Lague D, Brodu N, Leroux J. Accurate 3D comparison of complex topography with terrestrial laser scanner: application to the Rangitikei canyon (N-Z). *ISPRS Journal of Photogrammetry and Remote Sensing* 2013; **82**:10–26.
36. Teza G, Galgaro A, Zaltron N, Genevois R. Terrestrial laser scanner to detect landslide displacement fields: a new approach. *International Journal of Remote Sensing* 2007; **28**(16):3425–3446.
37. Rots JG. Comparative study of crack models. *Proceedings of the 3rd DIANA World Conference, Finite Elements in Civil Engineering Applications*, Tokyo, 2002.
38. Rots JG. Structural Masonry: An Experimental/Numerical Basis for Practical Design Rules. AA Balkema: Rotterdam, Netherlands, 1997.
39. Giardina G, Hendriks MAN, Rots JG. Sensitivity study on tunnelling induced damage to a masonry façade. *Engineering Structures* 2015; **89**:111–129.

DOI: 10.1002/stc